Supplementary Figures

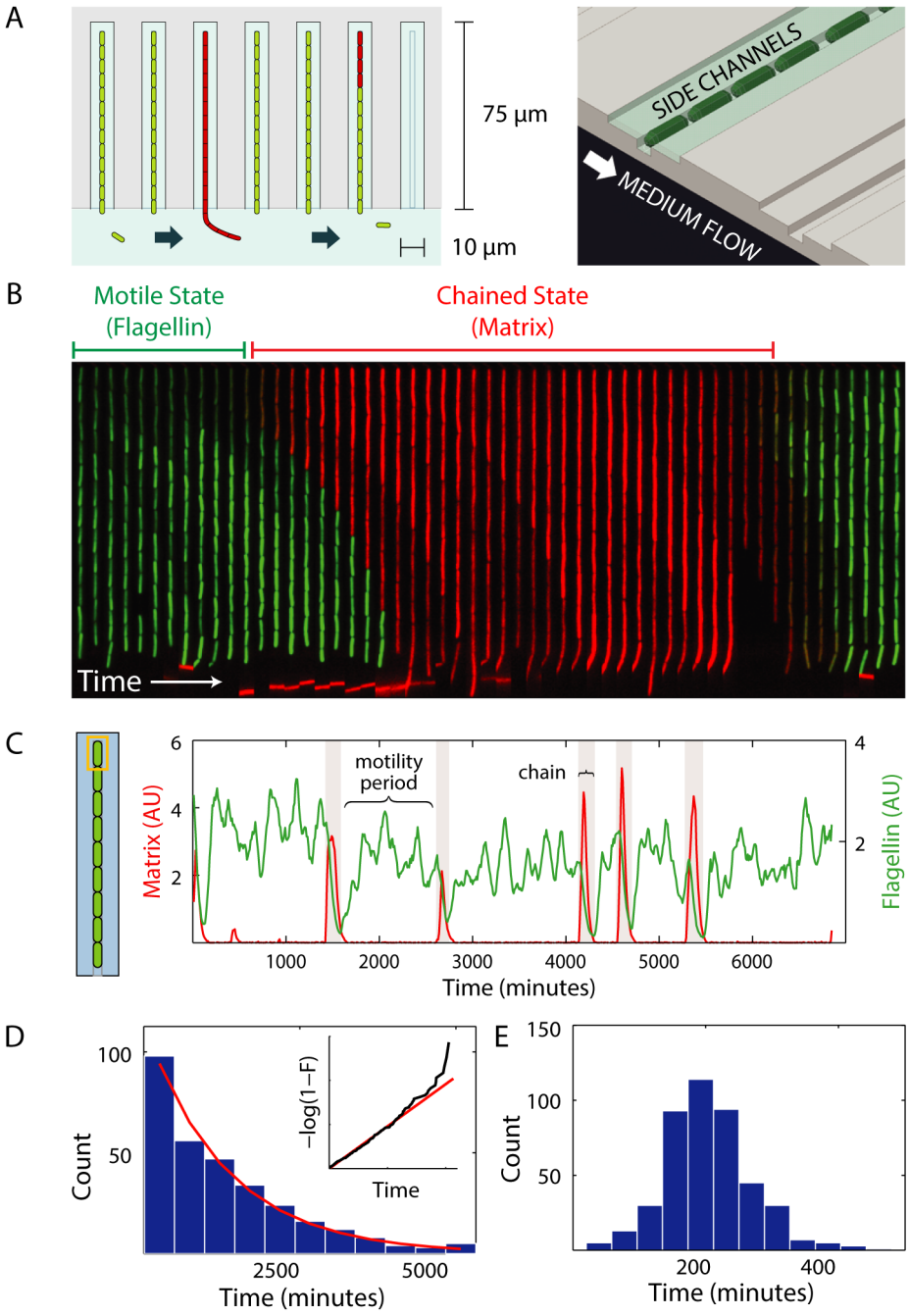

Fig S1. The *B. subtilis* swimming-chaining cell fate decision. During exponential growth, *B. subtilis* cells can choose to adopt a solitary, motile state or a sessile, chained state. In previous work, we characterized the stochastic dynamics of switching between these two states by tracking the behavior of hundreds of individual cells over hundreds of generations of growth under tightly-controlled conditions. This work revealed that residence in the motile state was memoryless, while commitments to the chained state were

tightly timed. All figures below are reproduced from Norman *et al* (*7*). **(A)** To observe switching dynamics under constant conditions, we grew *B. subtilis* cells in custom microfluidic devices. In our design, based on the 'mother machine', cells grow in narrow channels (~1.5 um across) that empty on one end into a feeding conduit (left panel, 'MEDIUM FLOW'). Cells at the far end of the channel (the 'mother' cells) push their progeny down the channel toward the medium flow. These daughter cells are eventually washed away, however the mother cells remain trapped indefinitely. We characterize the swimming-chaining decision by tracking the behavior of the mother cells. A crucial feature of our device was the installation of shallow 'side channels' on either side of the cell channel (right panel). These channels are too small for cells to enter, but allow for enhanced medium turnover across the length of the channel, ensuring that long chains of cells did not exhaust their medium supply. **(B)** Kymograph depicting an example chaining event. The mother cell grows for several divisions as a motile cell (i.e. expressing flagellin, 'Motile State'), before founding a chain (red cells, 'Chained State'). After several generations of growth, the chain synchronously disassembles into motile cells. Motile and chained cells are marked with transcriptional reporters for flagellin (green) and a matrix gene (red), respectively. **(C)** Example time trace of a single mother cell over ~300 generations of growth. The cell stochastically transitions between motile (high Flagellin, low matrix) and chained (low Flagellin, high matrix) states. **(D)** Histogram of motility period (left panel) durations. The distribution of motility periods is well-fit by an exponential distribution (red line), which is the hallmark of memoryless switching. Inset: log-transformed cumulative distribution of motility period durations. Under this transformation, an exponential distribution yields a straight line. The average time spent in a motility bout was 81 generations (~36 hours). **(E)** Histogram of chain durations. In contrast to motility, the residence times in the chained state are narrowly-distributed with an average of 7.6 generations. This narrow, unimodal distribution is indicative of timing: each cell that initiates a chain spends nearly the same amount of time in the state before switching back to motility. We speculate that this tight timing allows each cell to guarantee that a minimum community size is achieved before allowing for disassembly.

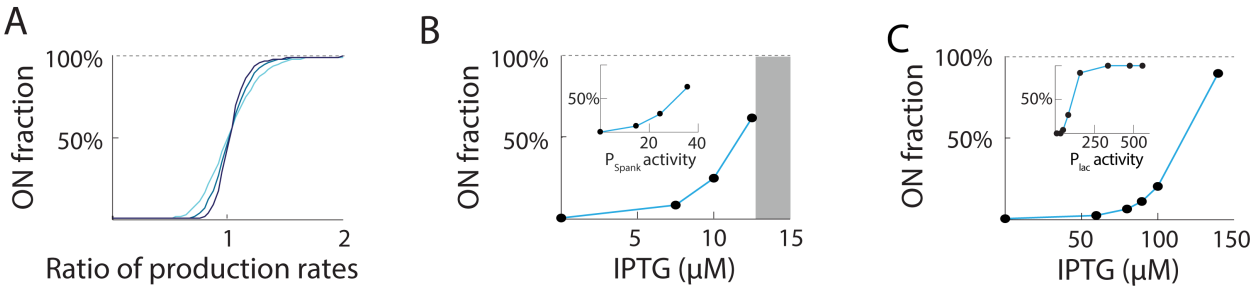

Fig S2. Stochastic competition generates ultrasensitive responses. A key quantity characterizing biological circuit function is the sensitivity of input-output relationships: for a given percentage change in an input, what is the percentage change in output? Much recent attention has been given to mechanisms that generate ultrasensitive responses, that is, outputs that exhibit changes of greater than x% for an x% change in input. As a comparison, a simple hyperbolic input-output relationship (i.e. as generated by Michaelis-Menten kinetics) produces at most a 1% change in rate for a 1% change, and would therefore not be described as ultrasensitive. In cases of extreme ultrasensitivity, responses can be described as 'switch-like', with outputs transitioning from zero to maximal intensity over a small range of input values. Molecular titration is a well-known mechanism for generating ultrasensitive responses. We therefore tested whether the SinI-SinR circuit produces ultrasensitive responses to changes in SinI expression. **(A)** Ultrasensitive responses to changes in the balance between *I* and *R* in the theoretical model of stochastic competition. Steady state fractions of time spent in the 'ON' state (i.e. $I > R$) are plotted for low (light blue), intermediate (dark blue) and high (black) average *I* and *R* abundances over a range of relative synthesis rates. **(B)** Average fraction of population in the 'ON' state as a function of IPTG concentration for the reduced *B. subtilis* strain (TMN-1159, Δ*sinI* Δ*slrR* P_{spank}-*sinI* P_{tapA}-*cfp* P_{hag}-*mKate2 hag233V*). The IPTG regime covered by the grey box was experimentally inaccessible due to microfluidic device clogging when cells overproduce matrix. Inset: average fraction of cells in the ON state plotted as a function of P_{spank} promoter activity. **C)** Average fraction of population in the 'ON' (i.e. GFP-positive) state as a function of IPTG concentration for the reconstituted *E. coli* system (NDL-423, Δ*clpXP* $P_{rpsOMod}$-*sinR* P_{lac}-*sinI* $P_{synthR1}$-GFP). Inset: average fraction of cells in the ON state plotted as a function of P_{lac} promoter activity, showing that ultrasensitivity is not a consequence of cooperativity of the Lac repressor (Materials and Methods, 'Measurement of fraction ON').

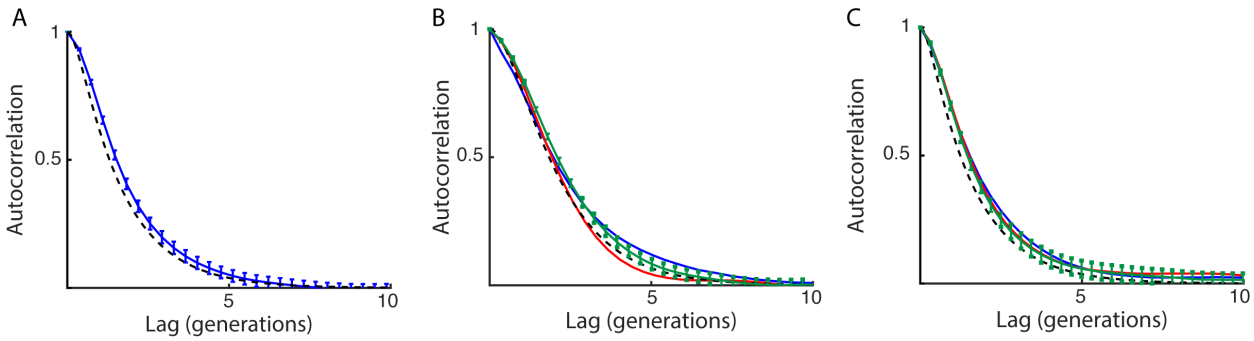

Fig. S3. Stochastic competition model captures reporter autocorrelations. The stochastic competition model predicts a specific shape for reporter autocorrelation functions (see SM section 'Expected autocorrelation in experimental reporters' for a detailed discussion). Here, we compare this prediction to the measured autocorrelations in reporter expression for the native, reduced *B. subtilis* and reconstituted *E. coli* circuits. Note that expected autocorrelation curves are parametrized by the fluorescent reporter maturation rate. These rates were taken from a recent systematic study of fluorescent protein maturation (*49*). **(A)** Autocorrelations in chaining reporter in the *slrR* mutant *B. subtilis* strain (blue curve, TMN-1158, Δ*slrR* P_{hag}-*mKate2* P_{tapA}-*cfp hagA233V*) and stochastic competition model (black, assumes a maturation half-time of 6.6 minutes for CFP). Error bars derived from bootstrapping are included for the *slrR* mutant data. Experimental data were collected in our previous study (*7*). **(B)** Autocorrelations in chaining reporter expression for the reduced *B. subtilis* strain (TMN-1159, Δ*sinI* Δ*slrR* P_{spank}-*sinI* P_{tapA}-*mKate2* P_{hag}-*gfp hag233V*) grown in 7.5 µM (blue), 10 µM (green) and 12.5 µM (red) IPTG. Error bars derived from bootstrapping are included for the 7.5 µM condition. Theoretical expectation for stochastic competition is plotted for comparison (dashed black curve, assumes a maturation half-time of 34 minutes for mKate2). **(C)** Autocorrelations in reporter expression for the *E. coli* reconstitution strain (NDL-423, Δ*clpXP* $P_{rpsOMod}$-*sinR* P_{lac}-*sinI* $P_{synthR1}$-GFP) grown in 90 µM (blue), 100 µM (green) and 110 µM (red) IPTG. Error bars derived from bootstrapping are included for the 90 µM condition. Theoretical expectation for stochastic competition is plotted for comparison (dashed black curve, assumes a maturation half-time of 5.6 minutes for GFPmut2).

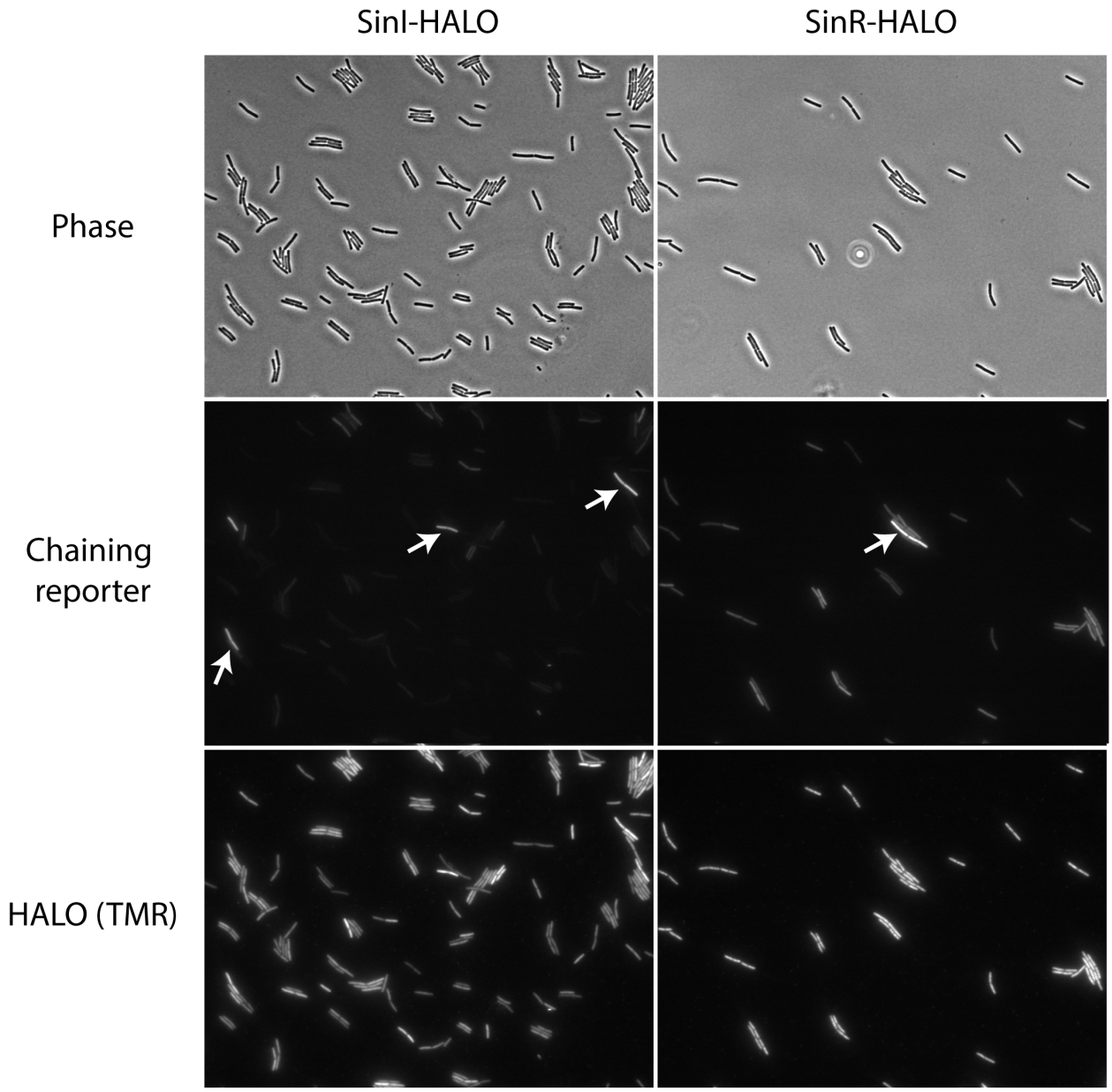

Fig S4. Stochastic activation of chaining reporter in HALO strains. To visualize endogenous SinI and SinR expression patterns, we complemented *sinI* and *sinR* null mutations with *sinI-HALO* or *sinR-HALO* genes under the control of the native promoters. We refer to these strains as TMN-1227 (*ΔsinI ylnF*/*yloA*::P_{sinI}-*sinI-HALO* (spc) P_{tapA}-*cfp*(Cm) *slr::tet*) and TMN-1229 (*sinR::mls ywrK*::P_{sinR} -*sinR-HALO* (spc) P_{tapA}-*cfp*(Cm) *slr::tet*), respectively. Both strains were grown to early log phase in LB medium, stained with HALO reagent (TMR fluorophore), spotted on agarose pads and imaged on phase contrast, TMR and CFP channels. We note that these cells lacked the *slr* gene, and so did not exhibit morphological signs of

chaining. Instead, we monitored the activity of SinR target genes through a P_{yqxm}-*cfp* transcriptional reporter ('chaining reporter'). Example cells stochastically expressing high levels of the chaining reporter are highlighted (white arrowheads).

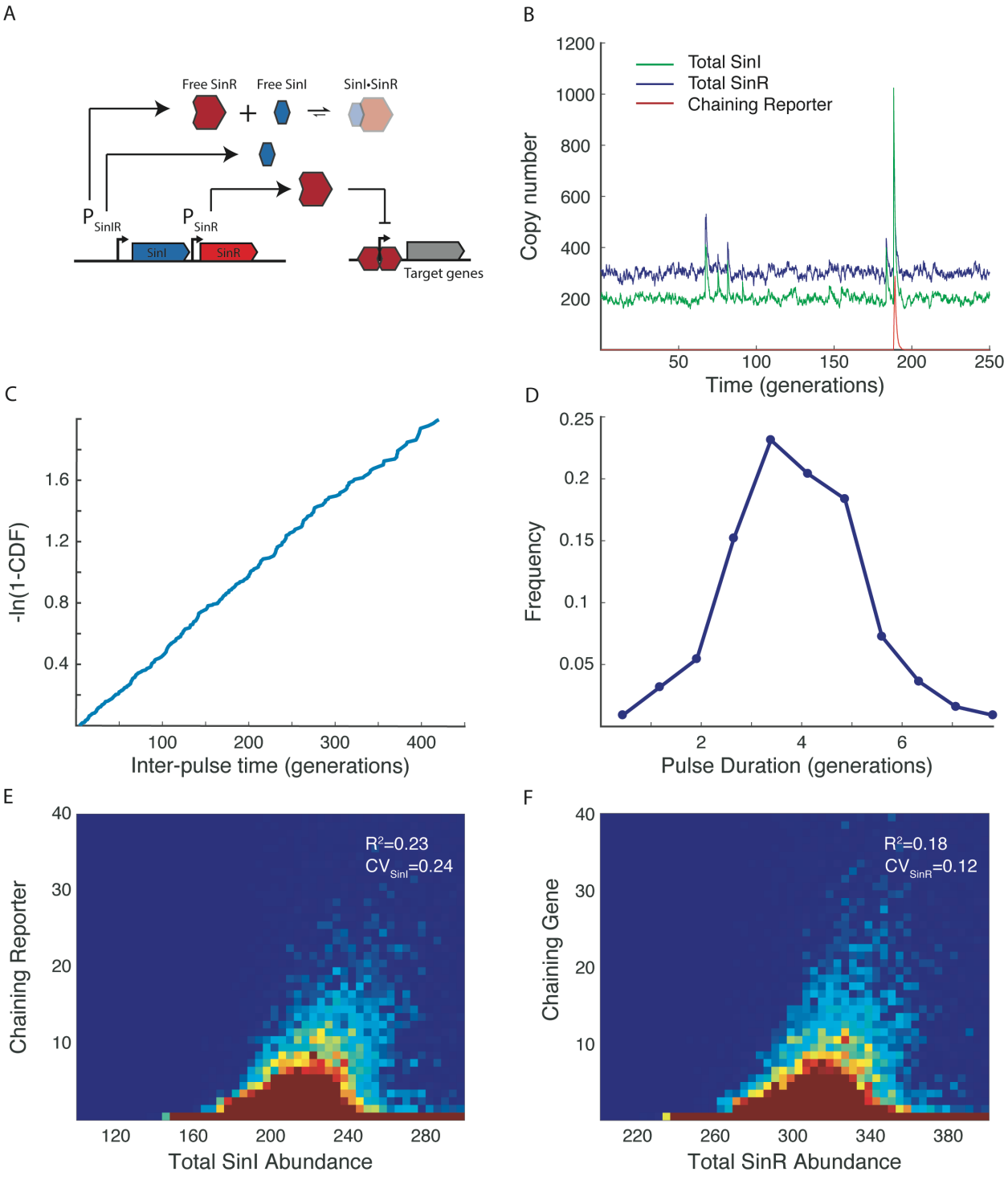

Fig. S5. Stochastic competition with SinI and SinR encoded in an operon. The simplest models of stochastic competition (e.g. with Poisson birth of both SinI and SinR) generate negative correlations

between SinR and the chaining reporter. However, we find a weak *positive* correlation between SinR and the reporter in *B. subtilis* cells (Fig. 2C). Here, we illustrate that this effect can be explained by the co-expression of SinI and SinR in an operon. Intuitively, this can occur when large, simultaneous bursts of SinI and SinR initiate a chaining event. Under these circumstances, both SinI and SinR abundances are higher than average when chaining reporter expression initiates. Notably, SinI and SinR can be expressed from a common promoter in *B. subtilis*. **(A)** Schematic of the simulation reactions. Three types of birth events are allowed: SinI and SinR together (top), SinI alone (middle) and SinR alone (bottom). Joint SinI-SinR birth events occur as geometrically-distributed bursts. SinI and SinR are removed from the system by first-order degradation. SinI-SinR complex formation is irreversible, and complexes are removed from the system by first-order degradation. When the free SinR concentration reaches zero, target gene expression occurs. Simulation details are described in the SI. **(B)** Example simulation time trace. Total SinI (SinI + SinI•SinR, green), total SinR (SinR + SinI•SinR, blue) and the chaining reporter (red) are shown. **(C)** Residence times in the reporter-negative (i.e. 'motile') state are exponentially distributed. Data are plotted as a log-transformed CDF. Under this transformation, an exponential distribution yields a straight line. **(D)** Residence times in the reporter-positive (i.e. chained) state are sub-exponentially distributed, indicating timing of commitments. **(E)** Total SinI abundance correlates positively with the chaining reporter abundance. Simulations were uniformly sampled in time to generate the scatter plot. **(F)** Total SinR abundance positive correlates with chaining reporter abundance. Simulations were uniformly sampled in time to generate the scatter plot.

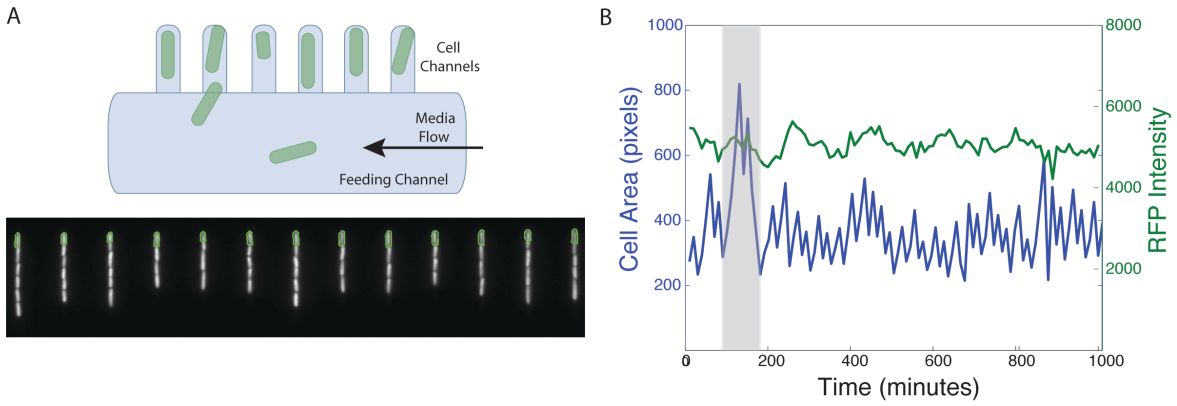

Fig. S6. Live cell imaging with the mother machine. (A) Upper panel: schematic of the mother machine device. The device comprises an array of 1.3 µm-wide channels that empty on one end into a central feeding channel. Cells trapped in the channels are fed diffusively from the fresh medium in the feeding channel, and also expel their progeny from the device by pushing them out into the flow. Under our experimental conditions, the entire device's medium supply is replaced between 5-10 times per minute. Lower panel: Example fluorescence (RFP channel) image of NDL-423 in the mother machine. Cell segmentation boundaries are plotted in green. Note that we only segment and track the uppermost cell in each channel—the 'mother'—as only these cells remain in the device throughout the experiment. **(B)** Example raw data trace from the mother machine. Cell size (blue) and segmentation marker intensity are plotted for a single lineage over the course of one experiment. Cell divisions are evident as sudden decreases in cell size. Spontaneous filamentation occasionally occurs (grey box) at frequencies consistent with previous observations in shaken culture.

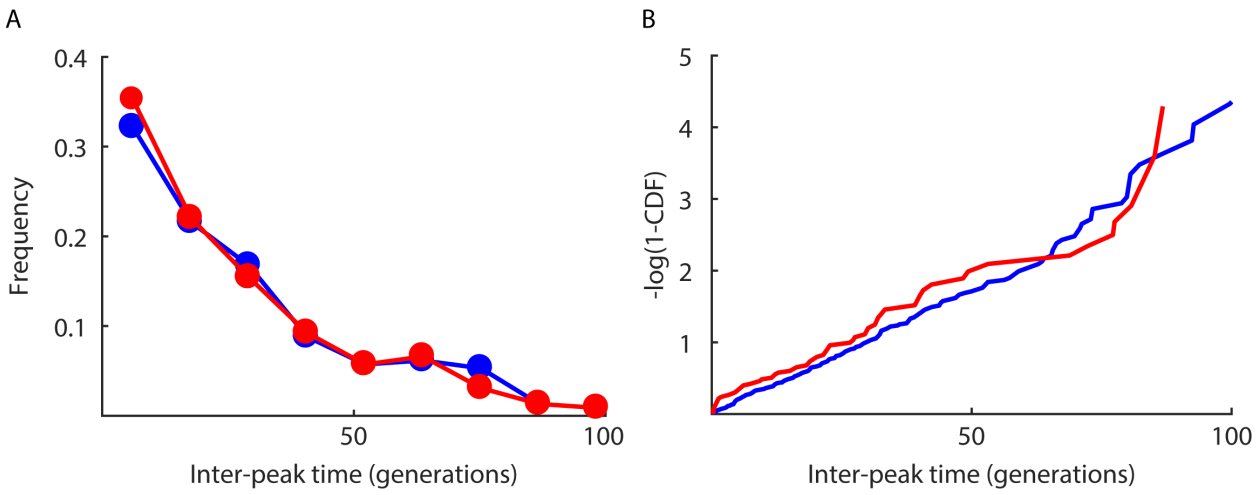

Fig. S7. SlrR plays no role in pulse initiation in the reduced *B. subtilis* circuit. In our previous study (*7*), we demonstrated that *B. subtilis* strains with wild type and *slrR* mutant chaining circuits initiated pulses of chaining reporter expression with indistinguishable distributions of inter-event times. To test whether SlrR is similarly dispensable for pulse initiation in the reduced circuit context, we measured matrix reporter dynamics in reduced circuit strains with (NDL-88, Δ*sinI* P_{spank}-*sinI* P_{tapA}-*cfp* P_{hag}-*mKate2 hag233V*) and without (TMN-1159, Δ*sinI* Δ*slrR* P_{spank}-*sinI* P_{tapA}-*cfp* P_{hag}-*mKate2 hag233V*) SlrR feedback. We grew both strains in the mother machine in the presence of 8.5 μM IPTG and compiled pulse firing statistics using the pipeline described in Figs. S18 and S19. **(A)** Probability density function of inter-peak times for the $slrR^+$ (red) and $slrR^-$ (blue) strains. **(B)** Log-transformed cumulative density functions for $slrR^+$ (red) and $slrR^-$ (blue) strains. Under this transformation, an exponential distribution yields a straight line.

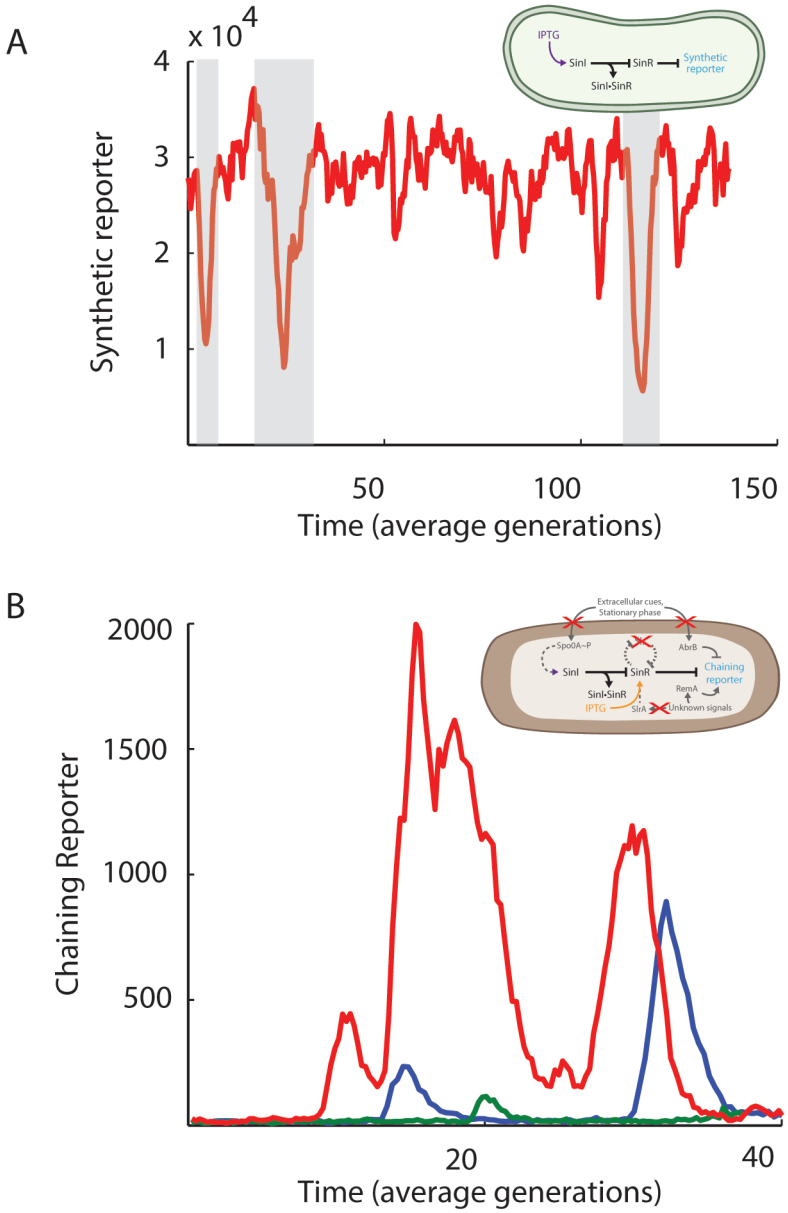

Fig. S8. Symmetry in the SinI-SinR system. (A) Inverse pulsing in the *E.* coli reconstituted circuit. In the presence of 200 µm IPTG, NDL-423 cells spend a majority of the time in the GFP-positive state, and repress the synthetic reporter only occasionally (grey boxes). This inverse pulsing reflects the inherent symmetry of the SinI-SinR system: with a sufficiently high IPTG concentration, SinI can be made the dominant species. **(B)** Cells bearing a deletion in *sinR* and an ectopic IPTG-inducible *sinR* gene (TMN1178, Δ*sinR ywrK*::P_{spank}-*sinR* P_{hag}-*gfp* P_{tapA}-*mKate2L hagA233V*) were imaged in the mother machine in the presence of 30 µM, 50 µM or 100 µM IPTG (red, blue and green curves, respectively). SinI was left under its native, constitutive regulation. Spontaneous pulses were observed in all three conditions, however the frequency and intensity of pulsing increased with decreasing IPTG concentration.

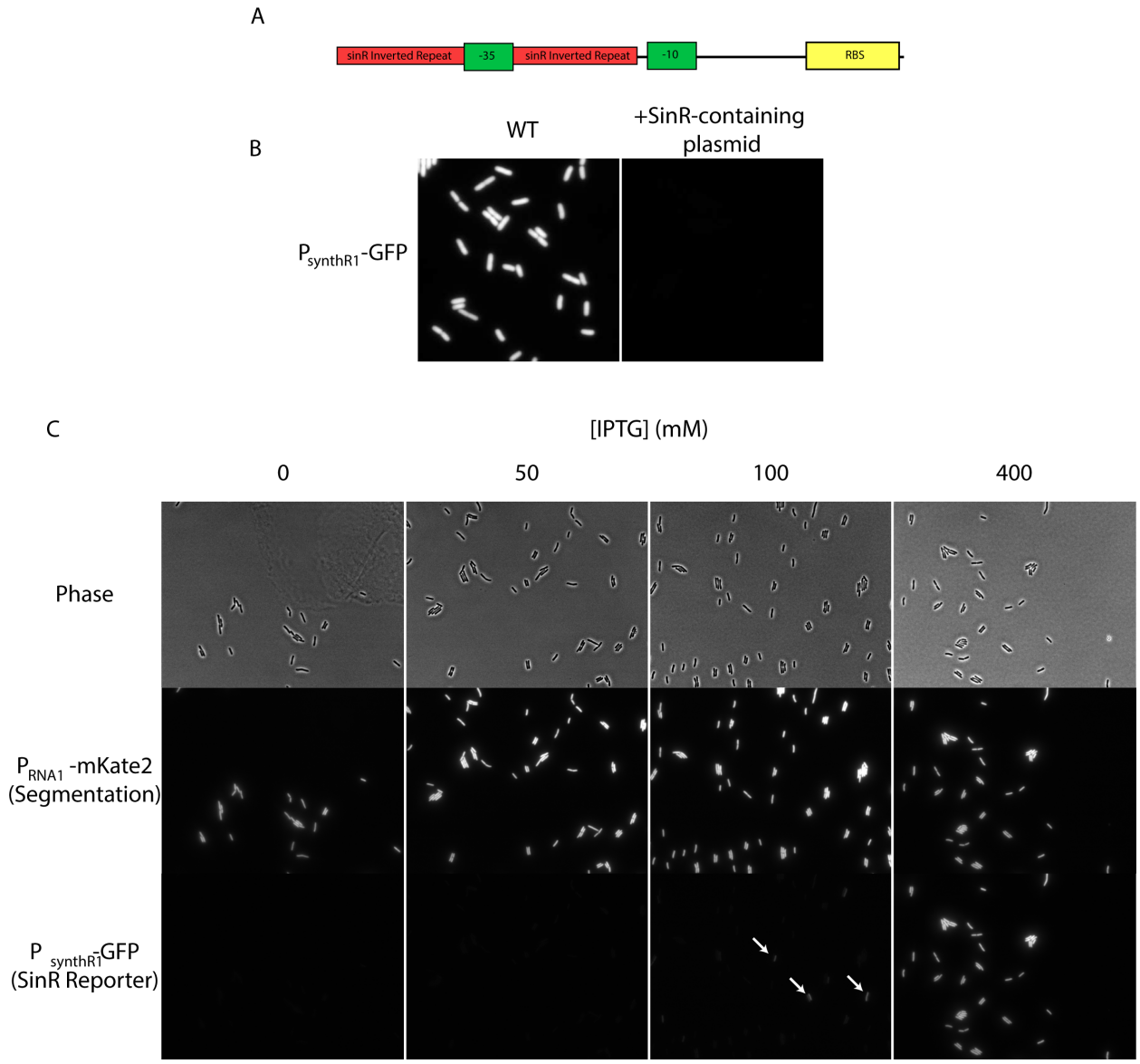

Fig. S9. $P_{synthR1}$ is effectively repressed by SinR. (A) Schematic of the $P_{synthR1}$ promoter. Expression is driven by the -10 and -35 elements of the λ P_L promoter. SinR repressibility is conferred by a pair of SinR target site inverted repeats (taken from the native *eps* promoter in *B. subtilis*) flanking the -35 element. **(B)** The $P_{synthR1}$-GFP reporter is strongly expressed in *E. coli* in the absence of SinR (left panel) and shut off when SinR is expressed from a plasmid (right panel). Pixel scaling is identical for the two images. **(C)** Expression of $P_{synthR1}$-*gfp* reporter with IPTG concentration. Reconstitution strain cells (NDL-423) were grown to early-log phase in LB supplemented with the indicated concentration of IPTG, spotted onto agarose pads and imaged. Pixel scaling is identical within each row. Arrowheads highlight rare cells that have initiated SinR reporter expression in intermediate IPTG concentrations.

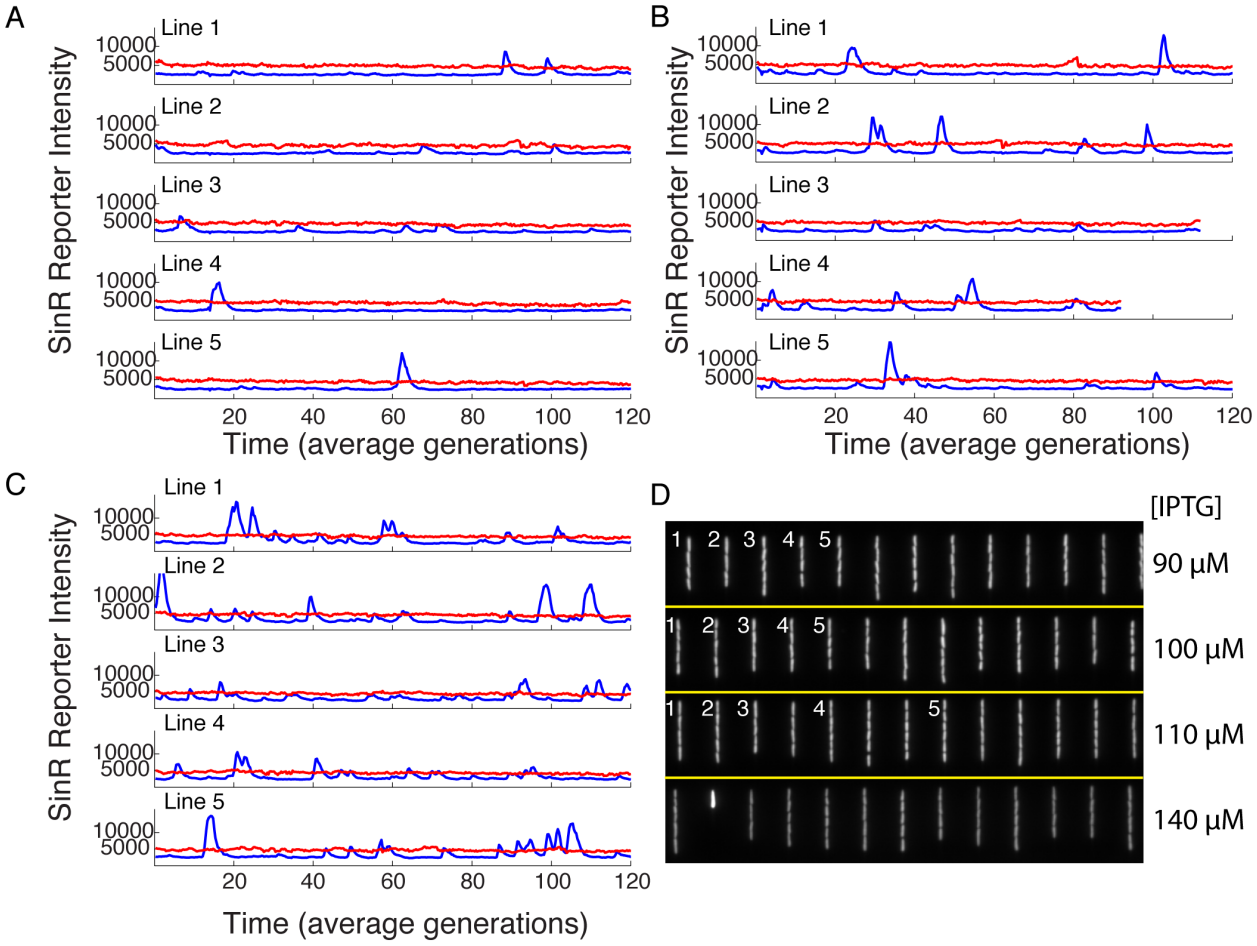

Fig. S10. Raw fluorescence traces from the reconstituted SinI-SinR circuit. All traces are drawn from the fields shown in Movie S2. In all panels, each sub-panel is an independent lineage and both the segmentation reporter (red) and SinR reporter (blue) are plotted. **(A)** Example traces from the reconstitution strain (NDL-423) grown in 90 uM IPTG. **(B)** Example traces from the reconstitution strain grown in 100 uM IPTG. **(C)** Example traces from the reconstitution strain grown in 110 uM IPTG. **(D)** Reproduction of the first frame from 'Segmentation Reporter' half of Movie S2. The lineages highlighted in panels a-c are labeled with the corresponding line number.

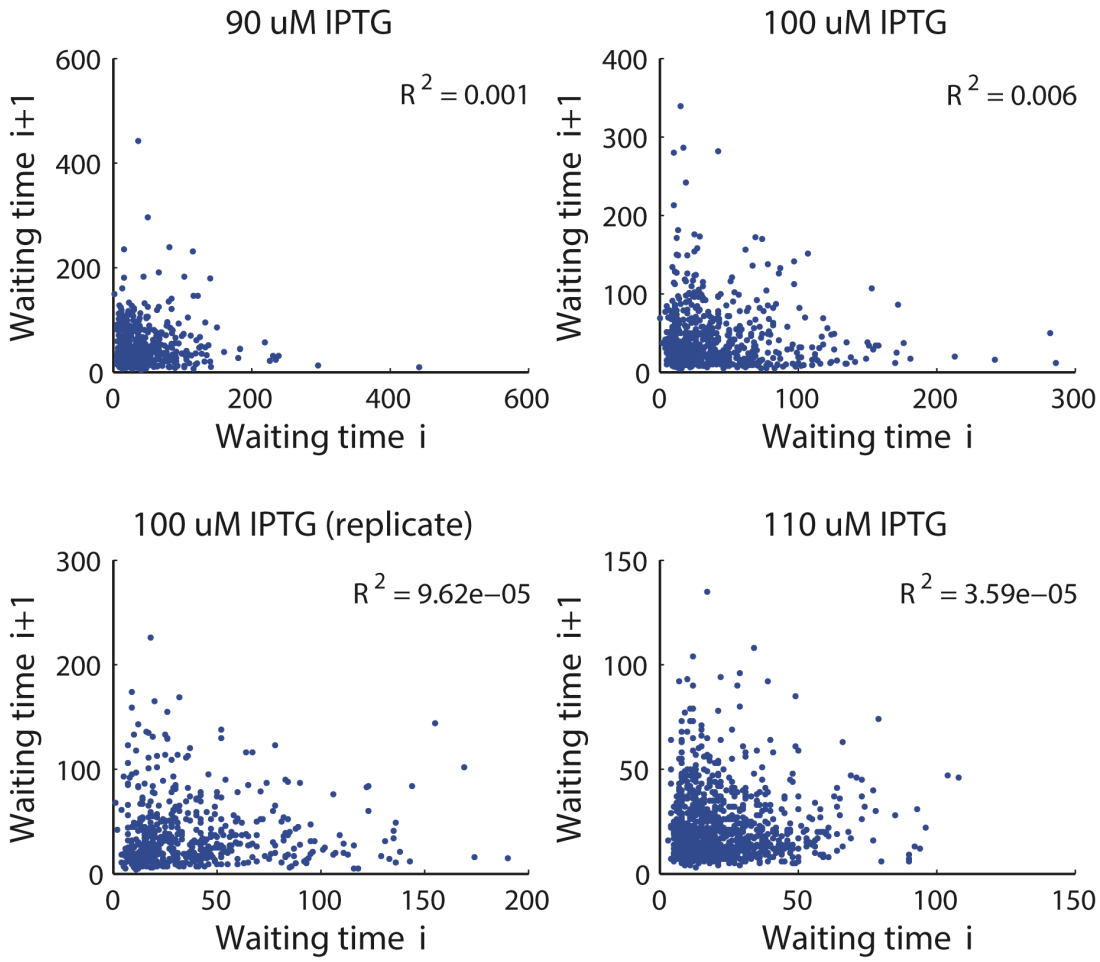

Fig. S11. Absence of correlation between subsequent excursions to the SinR-dominant state in the *E. coli* reconstituted circuit. In order to conclude that the transition from the SinR-dominant state to the SinI-dominant state is memoryless, we needed to confirm that residence times in the SinR-dominant state were exponentially-distributed (see Fig. 2J in the main text), and that successive residence times state were uncorrelated with one another. To satisfy the second requirement, here we scatter each pair of successive inter-peak times against one another for NDL-423 grown in 90 µM (upper left), 100 µM (upper right), 100 µM (replicate, lower left) and 110 µM (upper right) IPTG. In all cases, correlations are negligible, consistent with memoryless transitions from the SinR-dominant state.

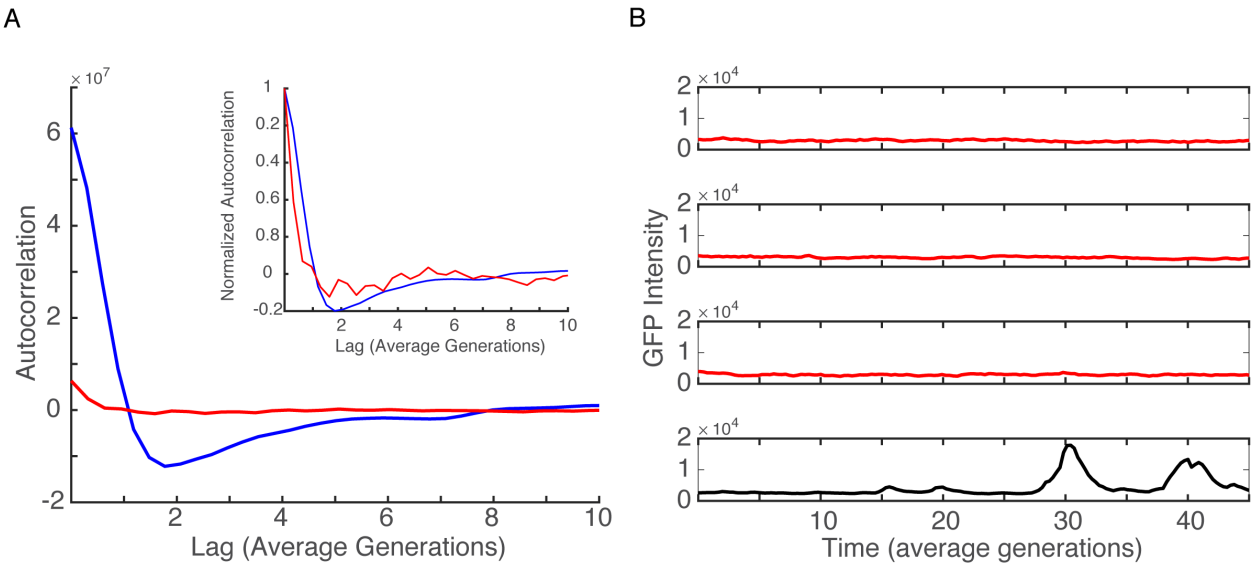

Fig. S12. Comparison of expression dynamics of P_{rpsO} and reconstituted SinI-SinR circuit. The multigenerational expression pulses generated by the SinI-SinR circuit are not present in the parent of the constitutive promoter driving SinR expression. **(A)** Raw (main panel) and normalized (inset) autocorrelations in d[GFP]/dt for the SinI-SinR reconstitution strain (NDL-423, grown in the presence of 110 uM IPTG) and a strain bearing a P_{rspO}-GFP transcriptional reporter (NDL-178). Data from the reconstitution strain and *rpsO* reporter strain are plotted in blue and red, respectively. Timed pulses of gene expression lead to a pronounced negative correlation (i.e. dip below zero) in the reporter derivative autocorrelation (See Supplementary Information section 'Inference of Pulse Timing from Autocorrelations' for details). This signature is present in the SinI-SinR circuit dynamics, but not in the *rpsO* reporter. The *rpsO* reporter curve instead reveals an absence of long-term correlations: the autocorrelation decays to zero within ~1 generation, and remains small for all subsequent lags. **(B)** Example lineages from the *rpsO* reporter strain (top three panels) and from the reconstitution strain (bottom panel).

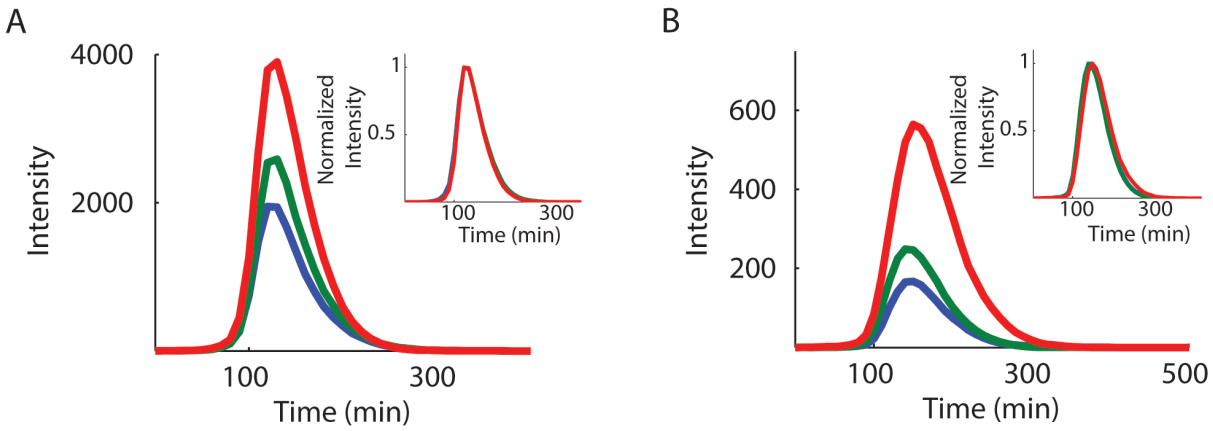

Fig. S13. Stereotyping of SinR target expression pulses. (A) Average pulse profiles of the synthetic SinR-responsive GFP reporter in NDL-423 (*E. coli* reconstituted circuit). Pulses from cells grown in 90 µM (blue), 100 µM (green) and 110 µM (red) IPTG were aligned along their leading edge and averaged (Materials and Methods). The average profiles can be precisely scaled onto one another by normalizing to the maximal value (inset). **(B)** Average pulse profiles of the P_{tapA} reporter in TMN-1159 (*B. subtilis* reduced circuit). Pulses identified in cells grown in 7.5 µM (blue), 10 µM (green) and 12.5 µM (red) IPTG were aligned along their leading edge and averaged as above. Again, the average profiles can be precisely scaled onto one another by normalizing to the average peak height (inset). We note that this scaling behavior is consistent with very short periods of SinI dominance. In this regime, the production of immature reporter proteins can be approximated as occurring in an instantaneous 'burst', and the resulting pulses of mature reporter differ primarily in their maximum heights.

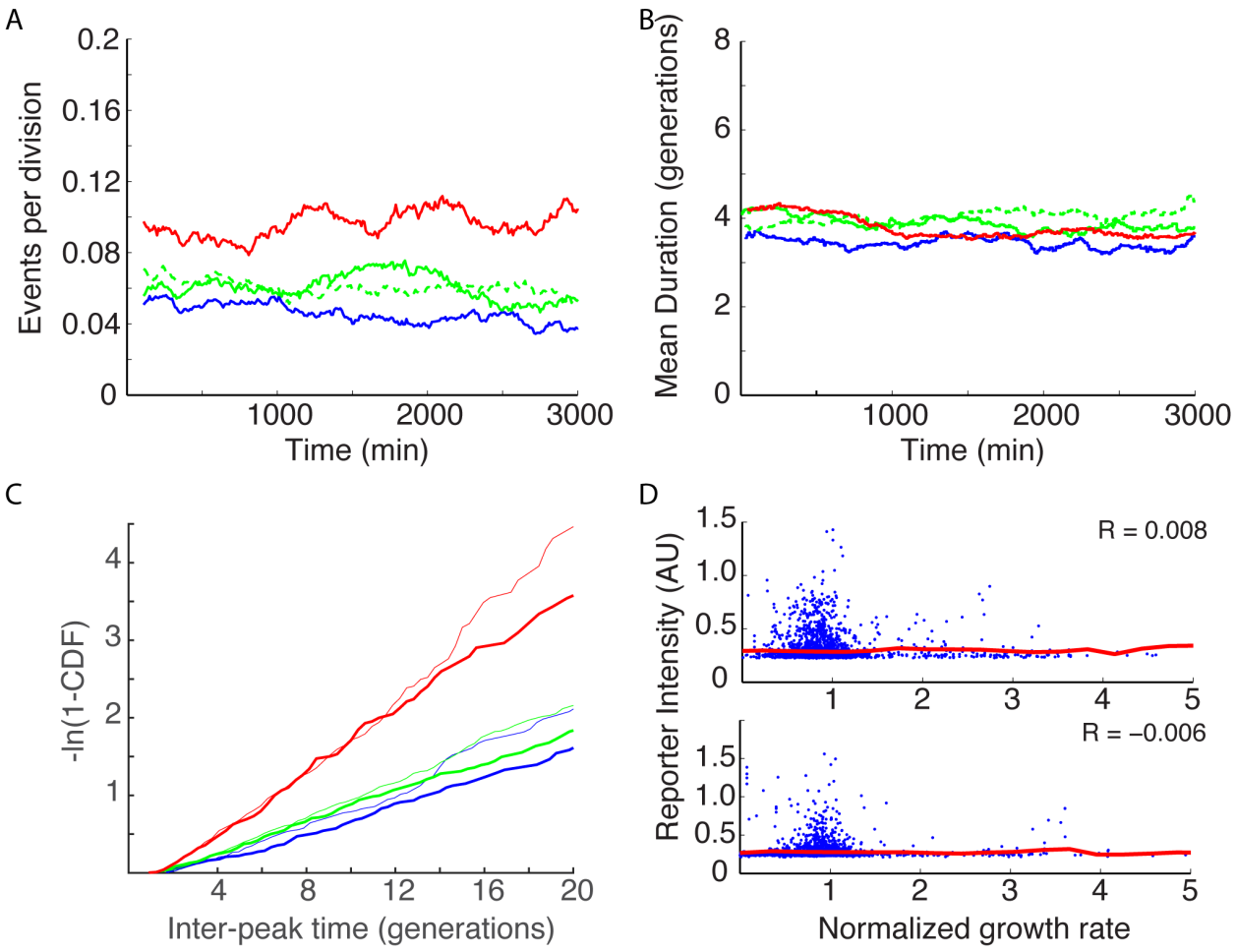

Fig. S14. Stationarity of pulse statistics in the reconstituted SinI-SinR circuit. (A) Stability of pulse frequency throughout each time-lapse experiment. A 25-frame sliding window average of the frequency of pulse initiations (number of pulses observed/number of divisions observed within the window) is plotted for the reconstitution strain (NDL-423) grown in 90 uM (blue), 100 uM (green) and 110 uM (red) IPTG. Two replicates for the 100 uM condition are plotted to facilitate comparison (cf. solid, dashed green curves). **(B)** Stability of pulse duration throughout each movie. A sliding window average of SinR reporter pulse duration is plotted for the reconstitution strain (NDL-423). Curve colors follow panel (A). **(C)** Stability of the distribution of inter-pulse times. The log-transformed CDF of inter-pulse times is plotted for the first half (thin lines) and second half (heavy lines) of each movie. Similarity of the distributions indicates that the pulse initiation characteristics are stable in time. Curve colors follow panels (A) and (B). **(D)** SinR reporter expression does not correlate with cell growth rate. SinR reporter intensity is scattered against the instantaneous growth rate for the reconstitution strain grown in 90 uM IPTG (upper panel) and 100 uM

IPTG (lower panel). Sliding window averages of reporter intensity are plotted to highlight bulk trends (red curves).

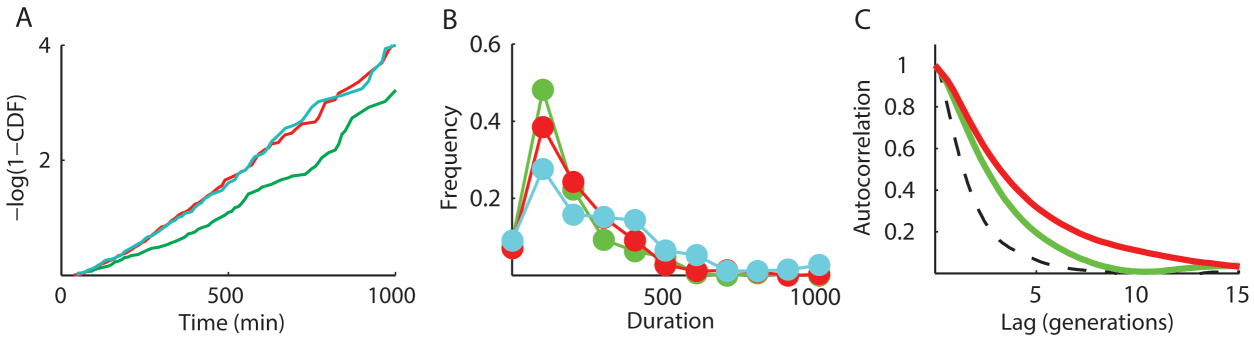

Fig. S15. Quantitative features of the *E. coli* SinI-SinR-SlrR reconstituted circuit. (A) Memoryless initiation of gene expression pulses in the presence of SlrR. Log-transformed distributions of inter-peak times for NDL-419 cells grown in 60 µM (green), 80 µM (red) and 100 µM (cyan) IPTG are plotted. Transformed in this fashion, an exponential distribution gives a straight line. **(B)** Distributions of SinR reporter peak duration in NDL-419 grown in 60 µM, 80 µM and 100 µM IPTG (green, red and cyan curves, respectively). **(C)** Autocorrelations in synthetic reporter expression in NDL-419 cells grown in 60 µM (green) and 80 µM (red) IPTG. The expectation for a model in which short periods of SinI dominance give rise to burst-like appearance of immature SinR reporter at memoryless intervals is plotted in black. We note that the slower decay of correlations in the presence of SlrR indicate long-lived bouts of SinR antagonism.

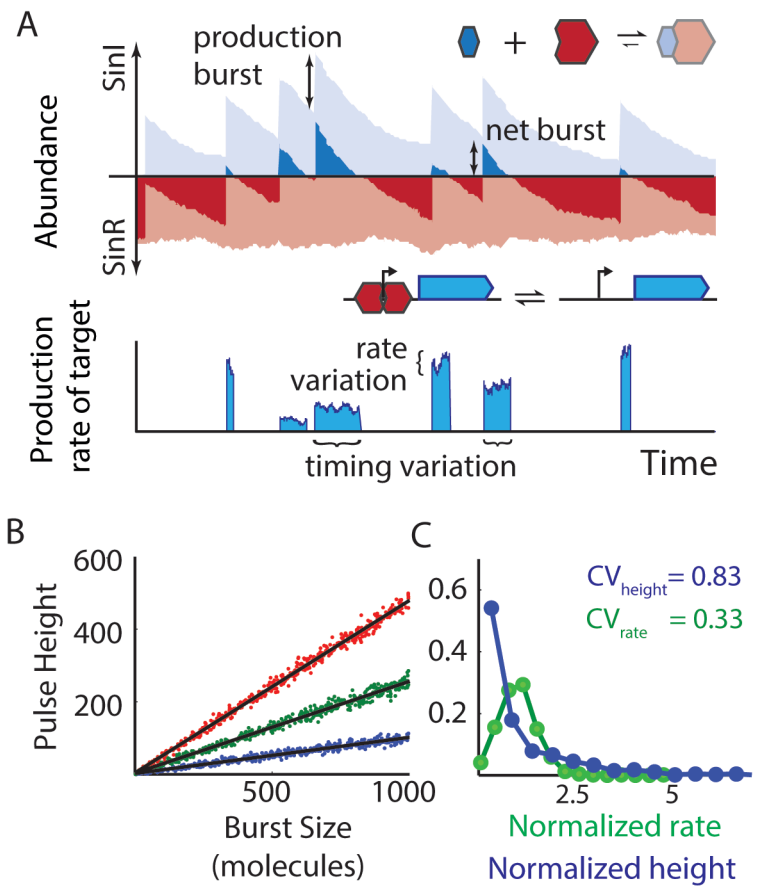

Fig. S16. Inferring timing of SinI dominance duration. (A) Schematic of sources of variation in SinR target gene expression. Upper cartoon: (reprinted from Fig. 3 in main text) cartoon of stochastic competition between SinI and SinR when SinI synthesis occurs in bursts. Free SinI and SinR levels are indicated in dark blue and red (respectively), while the amounts of bound SinI and SinR are indicated in light blue and red. Lower cartoon: Periods of SinI dominance initiate bursts of expression of SinR target genes. The total burst size in each event is a product of the duration of SinI dominance and the rate of target expression during this interval, but stochastic variation in each of these factors will lead burst sizes to fluctuate. 'Timing variation' occurs since SinI dominance arises from the stochastic antagonism mechanism we describe, and 'rate variation' occurs since gene expression is itself a stochastic process. **(B)** Peak height is proportional to SinR reporter burst size. Because of stochastic differences in dilution and maturation of fluorescent proteins, the distribution of burst sizes is not directly measurable. However, the height of each expression peak is proportional to the size of the burst of immature reporter that initiated it. We stochastically simulated the maturation and exponential dilution of bursts of immature reporter protein for a range of maturation:dilution rate ratios ($k_{mat}/k_{dilution}$ of 0.3, 1 and 3 for blue, green and red curves, respectively). In each case, the maximum height of each peak was proportional to the size of the initiating burst. **(C)** Estimating variability in the duration of SinI dominance periods. As noted above, burst size variation arises

from variation in the production rate of the reporter, and variability in the underlying period of SinI dominance. The latter factor cannot be directly measured, but can be connected mathematically to the observed burst size and rate variation distributions (see SM, Mathematical Derivations section 9), so we estimated those instead. Here we show the variability in peak height in NDL-423 grown in 110 μM IPTG (blue curve). As height is proportional to burst size, the CV, which is scale-invariant, will be the same. Variability in production rate was estimated by growing NDL-423 in saturating concentrations of IPTG (500 μM, green curve), so that cells were uniformly GFP positive but extrinsic variation in production rate would remain. In the figure, both curves were normalized to their respective averages to facilitate comparison. See Materials and Methods for details of calculation and experimental design, and for inferences regarding the variation in SinI dominance periods.

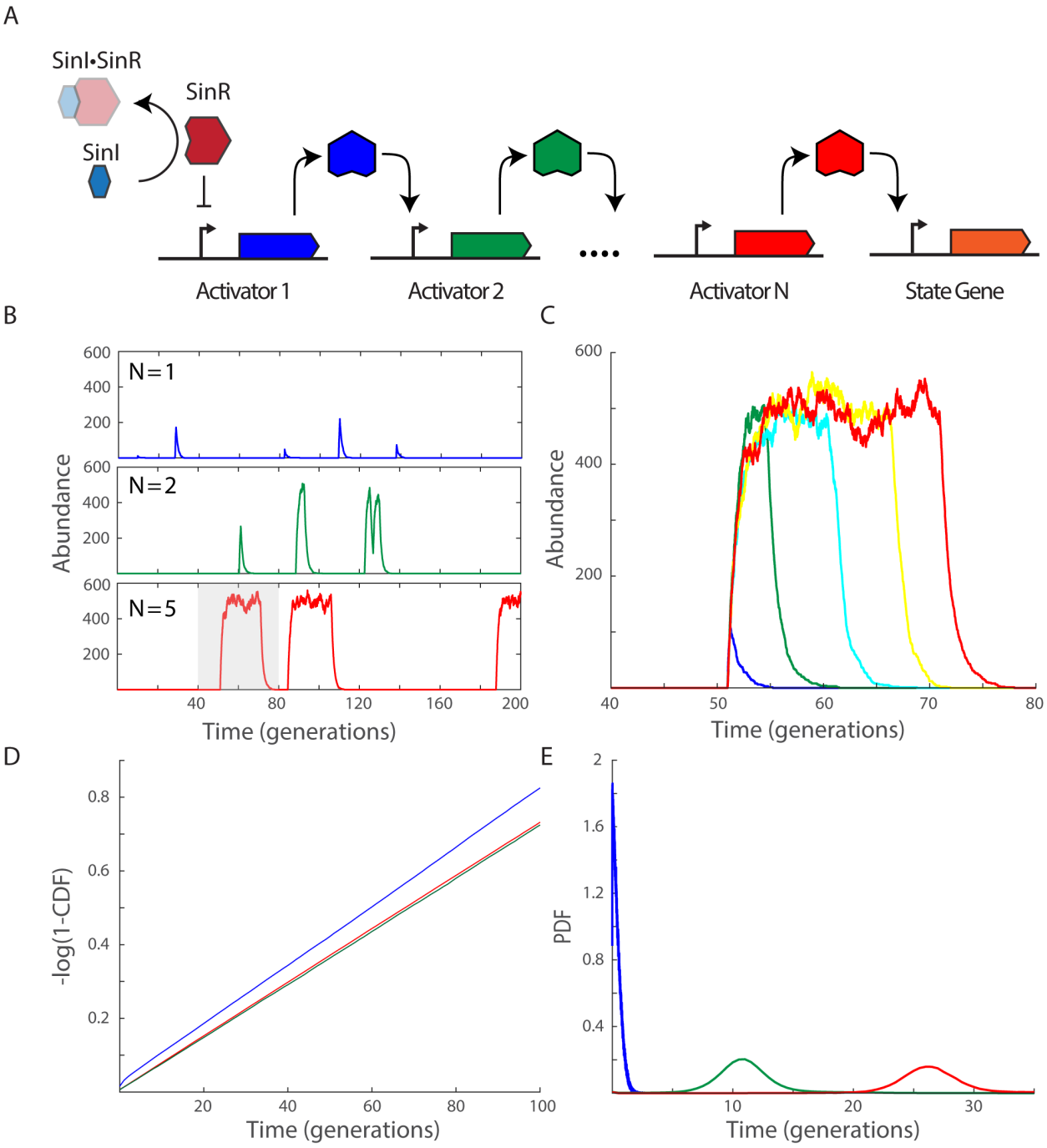

Fig. S17. A 'competition cascade' scheme extends commitments to ON state without feedback. In the simplest implementation, it is impractical for stochastic competition to create extended (e.g. > 10 generation) commitments to the alternate ('ON') state. Here, we demonstrate a simple principle that uses a cascade of activators to extended commitments to the ON state without feedback. **(A)** Schematic of the 'competition cascade' mechanism. In this scheme, SinR represses the gene for a transcriptional activator ('Activator 1'), which in turn activates the gene for another activator ('Activator 2'). At the end of this cascade, the final activator protein ('Activator N') drives the expression of genes corresponding to the

phenotype of interest (in our example, a chaining gene). Bouts in the ON state are initiated by stochastic competition between SinI and SinR, however commitment to the ON state is primarily governed by the number of steps in the cascade. (**B)** Simulated time traces for competition-cascade systems with one (blue), two (green) and five (red)-step cascades. The abundance of the terminal activator is plotted in each case. Bouts in the ON state are initiated by identical SinI-SinR competition systems. **(C)** Detailed mechanism of commitment extension. The abundance of each activator in the five-step cascade for the event shaded in the lower plot of panel B is plotted. Activators one, two three four and five are plotted in blue, green, cyan, yellow and red, respectively. In this simulation, all components are removed by dilution and each element of the cascade is activated by low concentrations of the upstream activator. Once expression of a given activator is initiated, it only begins to be cleared after the upstream activator is nearly completely gone. This allows each additional step in the cascade to add ~5 generations of commitment to the bout. **(D)** The competition cascade mechanism produces memoryless firing of bouts in the ON state. Log-transformed inter-peak time distributions are plotted for the one-step (blue), two-step (red) and five-step (green) cascades. **(E)** The competition cascade mechanism can produce tightly-timed commitments to the ON state. Peak duration distributions are plotted for cascades with one (blue), two (green) and five (red) activators.

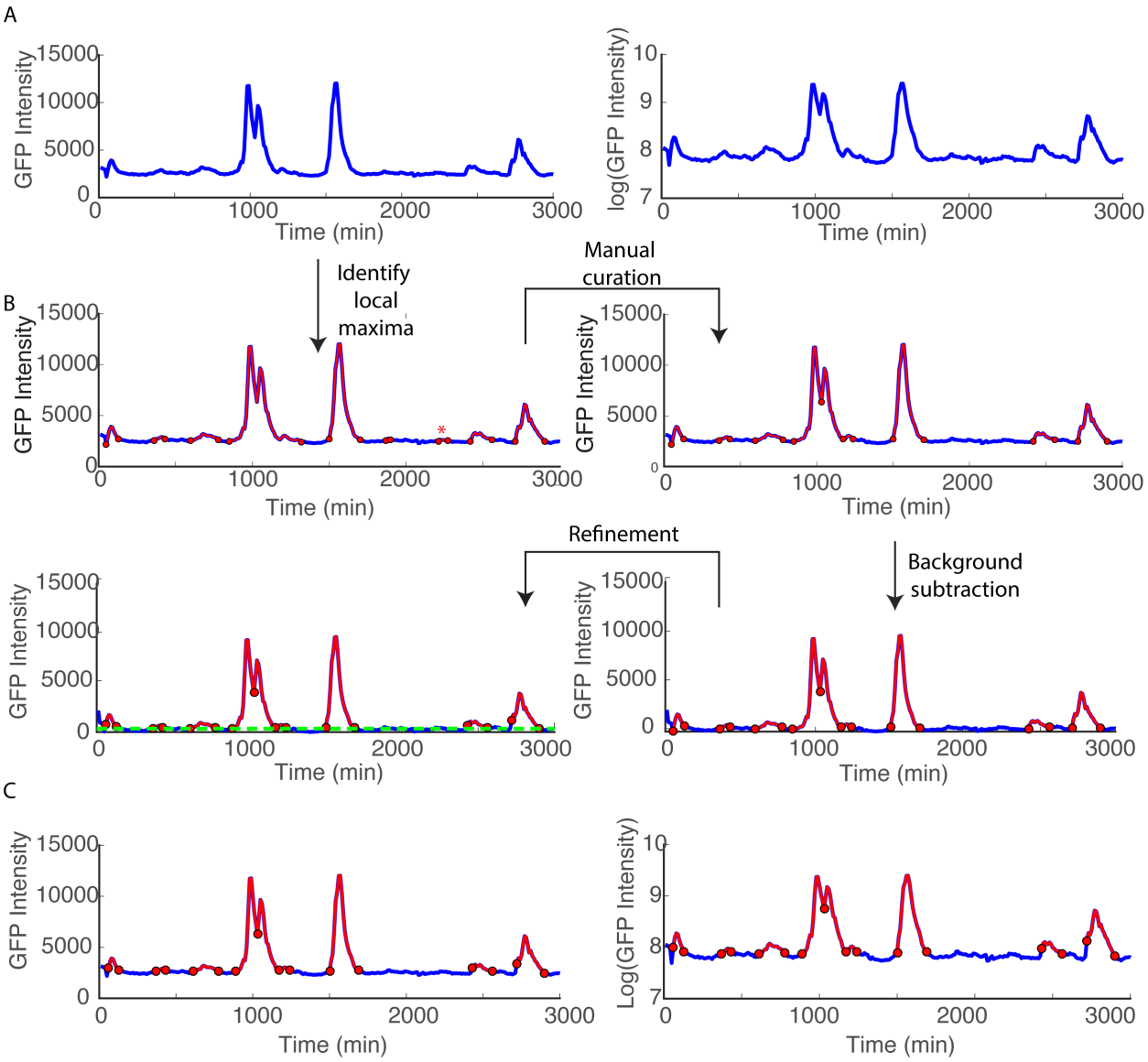

Fig. S18. Illustration of peak calling pipeline. (A) Example of raw data. A sample trace of $P_{synthR1}$-GFP expression from the reconstitution strain (NDL-423) grown in 100 μM is plotted in linear (left panel) and log (right panel) scales. **(B)** Step-by-step illustration of peak calling pipeline output. First, local maxima in the signal are identified, and approximate peak boundaries are identified (top left panel). Identified peaks are highlighted in red. Second, (top right panel) incorrect peak calls are manually corrected (e.g. asterisk highlights a peak that was removed from the data). Next, the fluorescence background signal is estimated via a 50-frame sliding window average of data that falls outside peaks and subtracted from the signal (bottom right panel; see Materials and Methods for details on background subtraction). Final peak

boundaries (bottom left panel) are then defined as the points at which each peak's signal unambiguously rises above fluctuations in the background signal (dashed green line, see Materials and methods for details on definition of this threshold). We note that the statistics of peak duration are insensitive to the threshold choice (see Fig. S19). **(C)** The final peaks are re-plotted on the raw fluorescence data from panel (A). Data are plotted in linear (left panel) and log (right panel) scales.

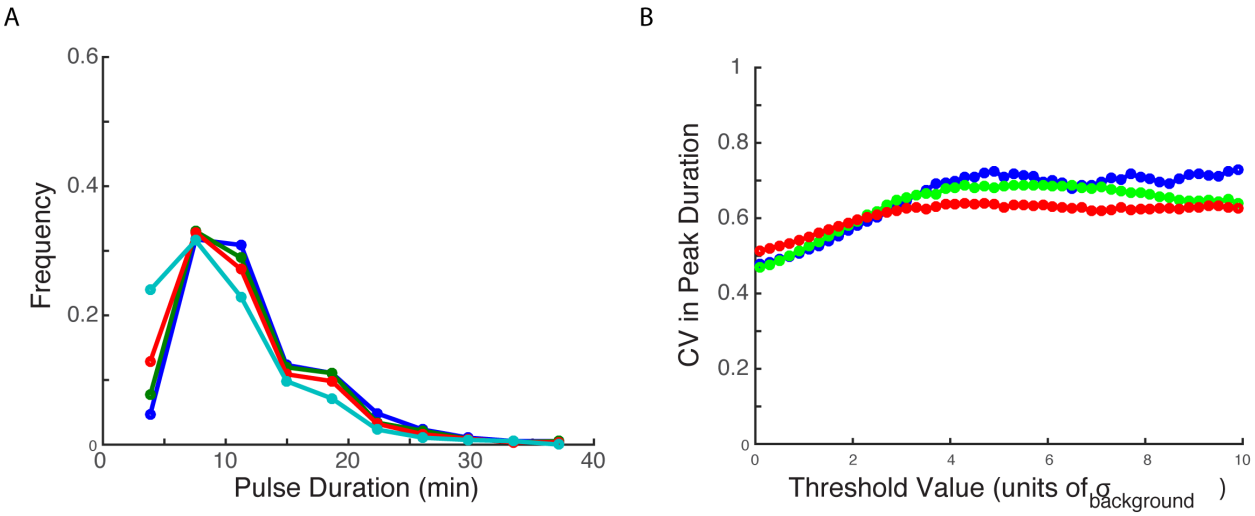

Fig. S19. Pulse statistics are insensitive to baseline threshold. The beginning and end of gene expression pulses were defined as the points where the SinR reporter intensity crossed a specified 'background' threshold. To demonstrate that the statistical properties of the peaks are not a result of this parameter choice, we recalculated the full distributions of peak durations for a range of threshold values. In all cases, we specify the threshold in units of $\sigma_{background}$, the standard deviation of cell intensities in the 'off' state (a measure of fluctuations in the fluorescence background, see Supplementary Methods for details). We note that figures in the main text were prepared with a threshold of 0.5 $\sigma_{background}$. **(A)** The distribution of SinR reporter pulse durations in the reconstitution strain (NDL-423) is insensitive to choice of baseline. Pulse duration distributions were recalculated with thresholds of 0.1, 0.5, 1 and 2 $\sigma_{background}$ (blue, green, red and cyan, respectively). **(B)** Peak timing is insensitive to threshold choice. Peak boundaries were defined with respect to a range of threshold values for the reconstitution strain (NDL-423) grown in 90 μM, 100 μM and 110 μM (blue, green and red curves, respectively). Distributions were narrower than exponential (i.e. CV < 1) for all tested thresholds.

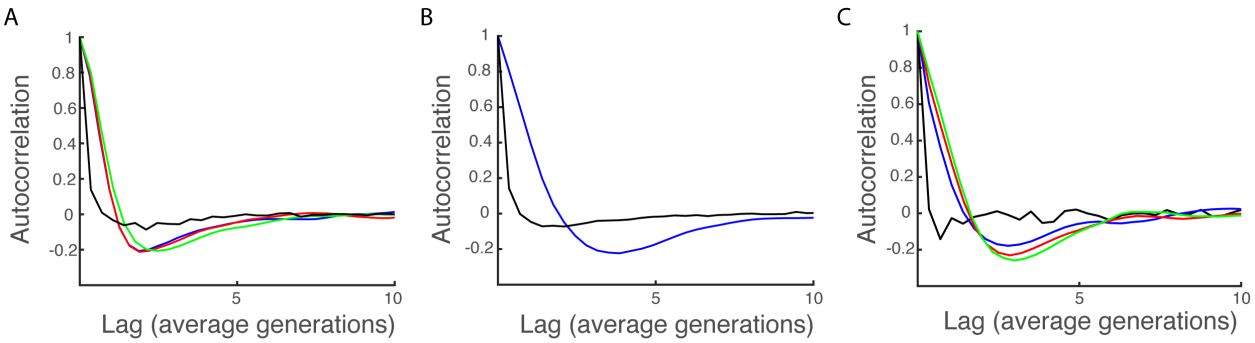

Fig. S20. Inference of pulse timing without calling discrete events. To ensure that our observation of timing in SinR target expression pulses was not due to errors or bias in our pulse identification pipeline, we looked for additional evidence of timing in the autocorrelations in reporter expression. If the pulses of gene expression are sub-exponentially distributed, the autocorrelation in dGFP/dt will have a marked 'dip' below zero at a lag set by the characteristic pulse duration (See Materials and Methods for details. 'Independent Inference of Pulse Timing' section). **(A)** Comparison of autocorrelations in d[GFP]/dt for the *E. coli* reconstitution strain (NDL-423) grown in 90 μM, 100 μM, and 110 μM IPTG (blue, red and green curves, respectively). For comparison, the autocorrelation in d[mKate2]/dt (i.e. the derivative in the constitutive segmentation reporter) is plotted in black. **(B)** Comparison of autocorrelations in d[mCherry]/dt (chaining reporter, blue curve) and d[YFP]/dt (constitutive segmentation marker, black curve) in the native *B. subtilis* circuit (TMN-1157. Data were gathered in (*7*)). **(C)** Comparison of autocorrelations in d[GFP]/dt for the reduced *B. subtilis* circuit (TMN-1159) grown in 0 μM,7.5 μM, 10 μM and 12.5 μM IPTG (black, blue, red and green curves, respectively). We note that no pulses occurred in the 0 μM condition. The characteristic 'dip' conferred by timed pulses of gene expression is therefore absent.

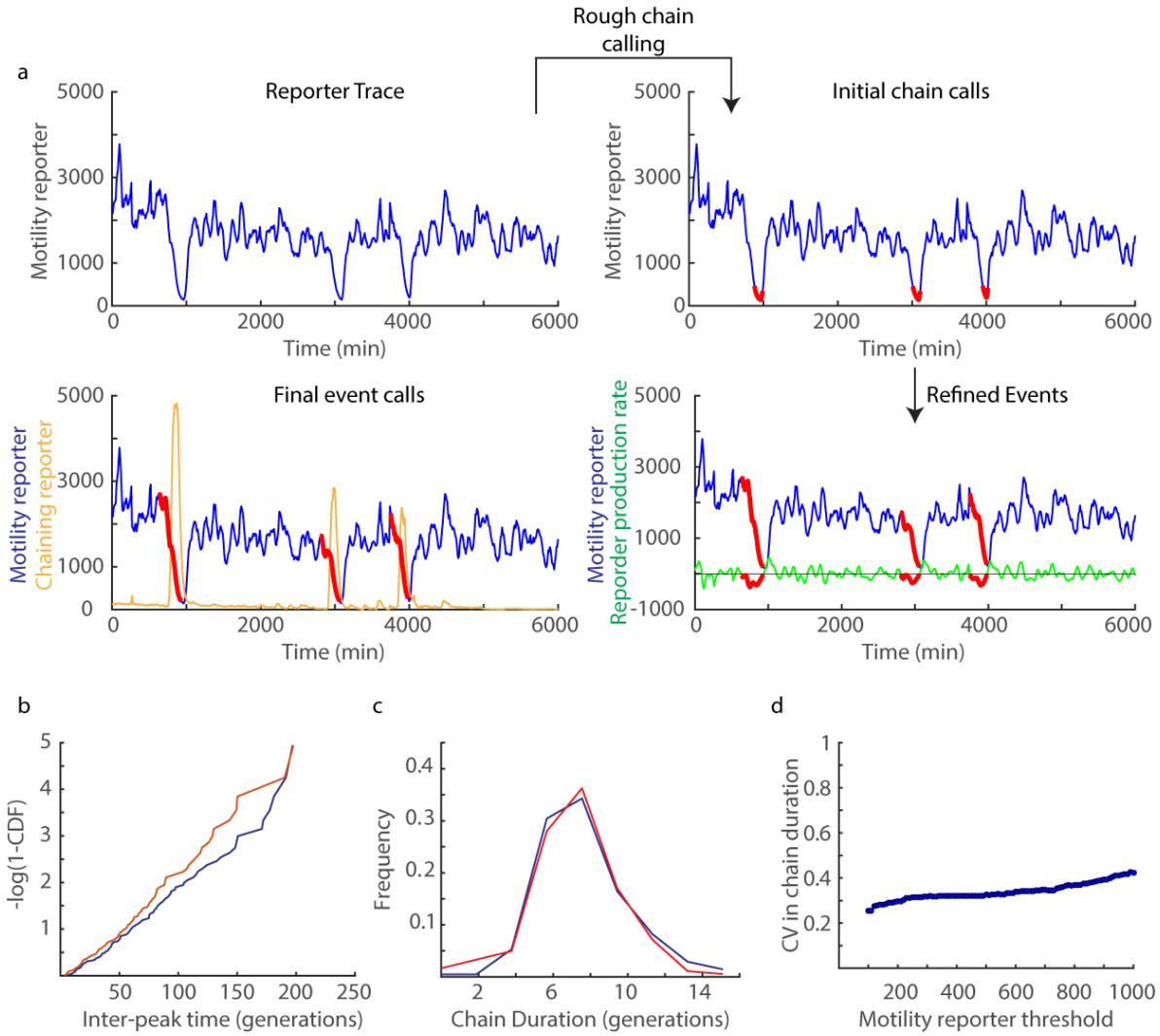

Fig. S21. Independent derivation of chaining statistics with motility reporter expression. To verify that our conclusions about the timed nature of the chained state in WT *B. subtilis* cells does not depend on our choice of chaining reporter, we repeated our analysis using only the motility reporter signal. As the chaining and motility programs are anti-correlated in the WT circuit, chaining events can be identified as pronounced dips in the motility reporter signal. All data are derived from TMN-1157 (see (*7*) for original dataset), which bears a WT chaining circuit (i.e. *sinI, sinR*, and *slrR* are all intact). **a,** Illustration of the modified event calling pipeline. Points at which the raw *hag* reporter trace ('Reporter Trace', upper left) drops below a pre-specified threshold are used to identify the rough locations of chaining events ('Initial chain calls', upper right. Chaining events are highlighted in red). Next, we refine the boundaries of the initial calls using the derivative in the *hag* reporter signal (lower right, 'Refined Events'). During each chaining event, *hag* expression is shut down, leading to a negative production rate for the *hag* reporter

(green curve). We define the boundaries of the chaining event as the points at which the *hag* production rate crosses from positive to negative (regions of negative hag activity are highlighted in red). The final event calls ('Final Event Calls', lower left)—derived *solely* from the *hag* signal—coincide well with the pulses of chaining reporter expression (orange curve). **b,** Comparison of inter-chain times for TMN-1157 derived from the chaining reporter (red) and motility reporter (blue). We find chaining initiation to be memoryless for both analysis methods. **c,** Comparison of chain durations for TMN-1157 derived from the chaining reporter (red) and motility reporter (blue). Similar distributions are obtained with both methods. **d,** Degree of observed chain timing is insensitive to choice of motility reporter threshold. We repeated the *hag* reporter-based chain calling for a wide range of threshold choices, and found that the distributions of chain durations exhibited timing (i.e. CV < 1) for all tested thresholds. All data in this figure were compiled with a motility reporter threshold of 500 AU.